Simulation of a Supersonic Jet Controlled by Plasma Actuators by the CESE Method

H. He,* S.-T. J. Yu,† G. Lou,‡ I. Adamovich, § and M. Samimy**

The Ohio State University, Columbus, OH 43202

This paper reports preliminary CFD of an ideally expanded supersonic jet controlled by localized arc filament plasma actuators. The space-time Conservation Element and Solution Element (CESE) method was employed to solve the three-dimensional Euler equations with and without the application of plasma actuators. A fully expanded Mach 1.3 jet from a 2.54 mm diameter round nozzle is used as the baseline jet. Four actuators evenly distributed around the perimeter of the nozzle are simulated by imposing energy pulses as a part of the upstream boundary conditions. Numerical results of four cases are reported: (i) the baseline jet without plasma actuator, (ii) simultaneous firings of four actuators at 9 kHz with the width (in the azimuthal direction) of each actuator of 3 mm, (iii) simultaneous firings of four actuators at 9 kHz with the width of each actuator of 1.5 mm, and (iv) simultaneous firings of four actuators at 4.5 kHz with the width of each actuator at 3 mm. In all cases, the thickness (in the radial direction) of the actuator is 1.5 mm and the power consumption of all actuators was less than 1% of the flow power. The two forcing frequencies of 4.5 and 9 kHz (St_D = 0.3 and 0.59) are within the jet column instability range. For Cases (ii) to (iv), numerical results clearly showed robust vortical structures generated in the controlled jet leading to significant mixing enhancement. The density and pressure fluctuation profiles have been completely changed as compared with that of the baseline jet.

I. Introduction

In the past, passive control of jets and mixing layers via geometrical modifications of nozzle/splitter plate trailing edge (e.g., using tabs, chevrons, lobbed nozzles) has been extensively studied. For active control, in general, one or more of the jet/shear layer instabilities must be manipulated, including the Kelvin-Helmholtz instability in the shear layer and the jet column or jet preferred mode instability. As the speed and the Reynolds number of the jet increase, so do the background noise, the instability frequencies, and the flow momentum. Therefore, actuators must provide excitation signals of much higher amplitude and frequencies.

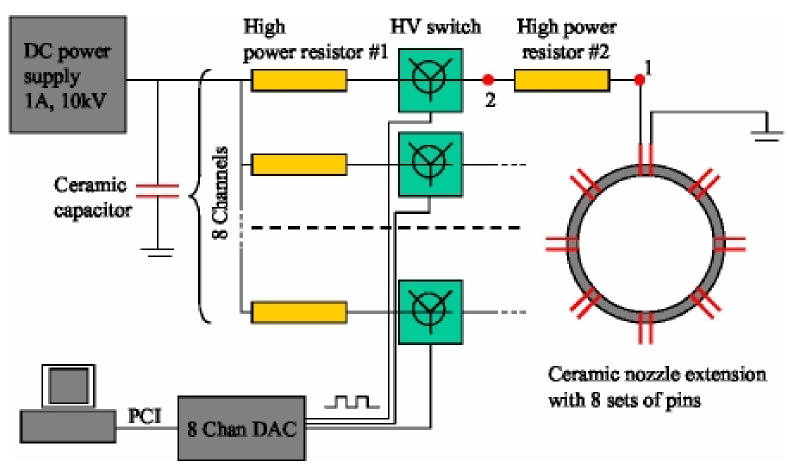

Figure 1.1: Schematic of LAFPA [3].

---

* Ph.D. Candidate, Department of Mechanical Engineering, and AIAA Student Member.
† Associate Professor, Department of Mechanical Engineering, and AIAA Member.
‡ Post Doctoral Researcher, Department of Mechanical Engineering, and AIAA Member.
§ Associate Professor, Department of Mechanical Engineering, and AIAA Member.
** Professor, Department of Mechanical Engineering, and AIAA Member.

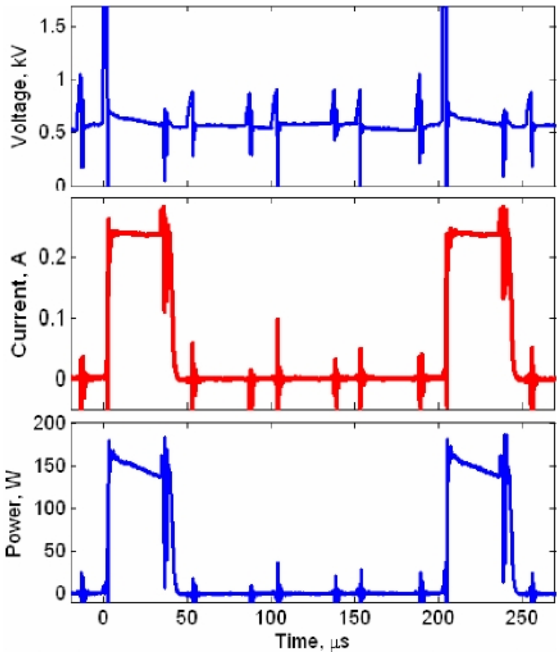

Figure 1.2: Time-dependent voltage, current, and power in a plasma actuator operated at 5 kHz frequency and 20% duty cycle.

Recently, Samimy et al. [1-3] have developed Localized Arc Filament Plasma Actuators (LAFPA) for excitation signals of high amplitude and high frequency to control high-speed and high Reynolds number flows. A brief description of the experiments reported in [1-3] is provided here. The ambient air is compressed, dried, and stored in two cylindrical tanks at a pressure of up to 16 MPa with a capacity of 36 m^3. The compressed air is supplied to the stagnation chamber and conditioned before entering into a Mach number 1.3 axisymmetric converging-diverging nozzle, which is designed using the method of characteristics for uniform flow at the nozzle exit. The air is discharged horizontally through the nozzle into an anechoic chamber. The nozzle has an exit diameter of 2.54 cm. A nozzle extension, made of boron nitride, was attached to the exit of the nozzle to house the plasma actuators. The actual Mach number of the jet was measured to be about 1.35.

Each actuator consists of a pair of pin electrodes. The electrodes are distributed around the nozzle perimeter (Fig. 1.1). A ring groove of 0.5 mm deep and 1 mm wide located approximately 1 mm upstream of the nozzle exit plane houses the electrodes and shields and stabilizes the plasma. In earlier experiments, the plasma was blown away without such a groove. In the latest work, the nozzle extension was made of boron nitride and steel piano wires of 1 mm diameter were used for electrodes. Measured center-to-center, the spacing between a pair of electrodes for each actuator is 3 mm, and the distance between the neighboring electrodes of two adjacent actuators is 6 mm. Figure 1.2 shows typical output of the plasma actuators in terms of voltage, current, and power.

Experimental results in [1-3] have clearly shown that the LAFPA can effectively change the flow structure of high-speed jets with a minute amount of energy input. To further understand the flow physics, this paper reports CFD results of the supersonic jets modulated by plasma actuators. The rest of the paper is organized as follows. Section 2 provides a brief description of the CESE method used in the present work. Section 3 presents the results and discussions. We then provide the concluding remarks and the cited references.

II. The CESE Method

In order to faithfully track all linear and nonlinear waves, the numerical method employed must be able to capture all interactions between time marching terms and nonlinear flux terms, which give rise to the generalized Riemann problem involving multiple waves propagating at different speeds according to the eigenvalues of the coefficient matrixes of the Euler equations.

For high-fidelity solutions, we use the CESE method [4-15], which is a novel numerical framework for all hyperbolic conservation equations. Previously, by using the CESE method, we have reported a wide range of highly accurate solutions, including detonations, cavitations, complex shock waves, turbulent flows with embedded dense sprays, dam breaking flows, MHD flows, aeroacoustics, nonlinear waves in solids, etc. For conciseness, we will only illustrate the basic ideas of the CESE method in the present paper. To proceed, we consider the Euler equations for gas dynamics:

$$\frac{d\mathbf{U}}{dt}+\frac{d\mathbf{E}}{dx}+\frac{d\mathbf{F}}{dy}+\frac{d\mathbf{G}}{dz}=0 \qquad (1)$$

Let $x_1 = x$, $x_2 = y$, $x_3 = z$ and $x_4 = t$ as the coordinates of a four-dimensional space-time Euclidean space E_4. By using the divergence theorem, the Euler equations become

$$\oint_{S(V)} \mathbf{h}_m \cdot d\mathbf{s} = 0\,, \qquad m=1,2,\ldots,5 \qquad (2)$$

where *S(V)* is the surface of an space-time region *V* in E_4, $d\mathbf{s}$ is a surface element vector pointing outward, and $\mathbf{h}_m$ is the space-time current density vector. Equation (2) states that the total space-time flux $\mathbf{h}_m$ leaving volume *V* through *S(V)* must conserve. The CESE method integrates Eq. (2) in E_4 and solves for the flow variables **U** at each new time level.

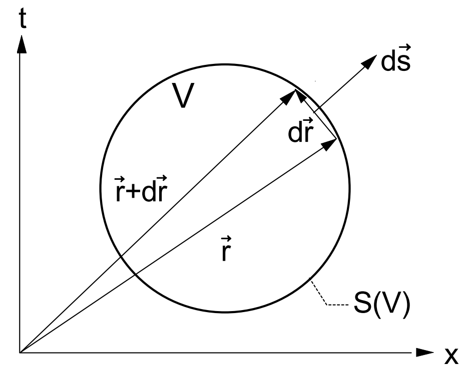

Fig 2.1: A schematic of space-time integral of the CESE method.

To integrate Eq. (2), the CESE method employs separate definitions of conservation element (CE) and solution element (SE). CEs are non-overlapping domains such that flux conservation is enforced over each CE, or over a union of neighboring CEs. Inside each CE, flow discontinuity is allowed. SEs are non-overlapping space-time domains such that within a SE flow variable and fluxes are assumed continuous and they are approximated by the first-order Taylor series expansion. We note that flow variables and fluxes could be discontinuous across neighboring SEs. In general, SEs do not coincide with CEs.

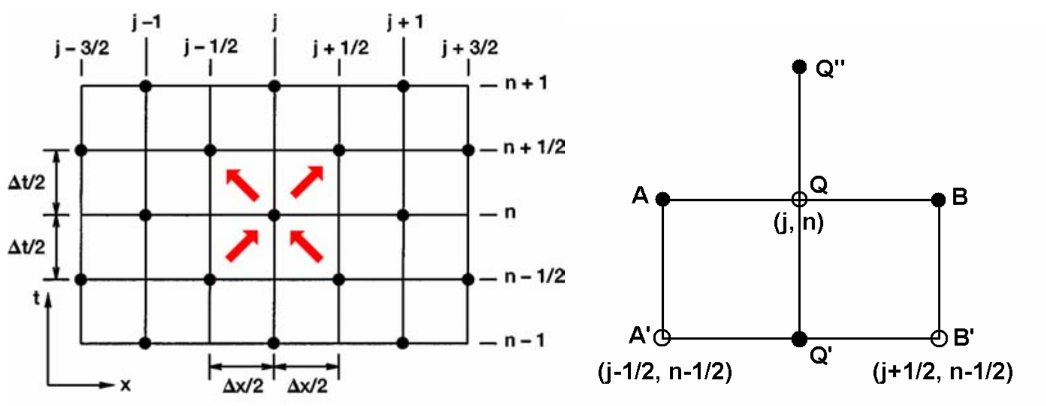

(a) (b)

Fig. 2.2: Schematics of the one-dimension CESE method. (a) The staggered space-time mesh and (b) SE (*j*, *n*) and CE (*j*, *n*).

For conciseness, the discussion of the numerical solution of Eq. (1) will be restricted to one spatial dimension in this paper. Figure 2.1 is a schematic for space-time flux conservation delineated by Eq. (2). The actual integration of Eq. (2) over a space-time domain, i.e., *S(V)* in Fig. 2.1, is done by discretizing the space-time domain as shown in Fig. 2.2, in which time marching of the CESE method is based on a space-time staggered mesh such that the flow information propagates only in one direction across the interfaces of neighboring CE and towards the future. The integration of Eq. (2) is performed without encountering a Riemann problem.

Figure 2.2(b) shows the CE and the SE associated with grid node (*j*, *n*). The SE is composed of two line segments: Q'Q" and AB, and their immediate neighborhood. The CE is the rectangle ABB'A'. For any (*x*, *t*) within SE(*j, n*), $u_m(x, t)$ and $f_m(x, t)$ are discretized based on the first-order Taylor expansion and they are denoted by the superscript *:

$$u_m^*(x,t;j,n) = (u_m)_j^n + (u_{mx})_j^n (x - x_j) + (u_{mt})_j^n (t - t^n)\,, \qquad (3)$$

$$f_m^*(x,t;j,n) = (f_m)_j^n + (f_{mx})_j^n (x - x_j) + (f_{mt})_j^n (t - t^n)\,. \qquad (4)$$

$$\mathbf{h}_m^*(x,t;j,n) = (f_m^*(x,t,j,n), u_m^*(x,t,j,n))\,. \qquad (5)$$

Equation (2) is then approximated by the discrete form:

$$\oint_{S(CE)} \mathbf{h}_m^* \cdot d\mathbf{s} = 0 \cdot \tag{6}$$

Without providing the details, we substitute Eqs. (3-5) into Eq. (6) and get

$$(u_m)_j^n = \left[(u_m)_{j-1/2}^{n-1/2} + (u_m)_{j+1/2}^{n-1/2} + (r_m)_{j-1/2}^{n-1/2} - (r_m)_{j+1/2}^{n-1/2} \right] / 2, \tag{7}$$

where

$$(r_m)_j^n = (\Delta x/4)(u_{mx})_j^n + (\Delta t/\Delta x)(f_m)_j^n + (\Delta t^2/4\Delta x)(f_{mt})_j^n \cdot \tag{8}$$

Equations (7-8) are the algorithm for solving u_m.

In two spatial dimensions, the computational domain is divided into non-overlapping quadrilaterals. Refer to Fig. 2.3(a). Vertices and centroids of quadrilaterals are marked by dots and circles, respectively. Q is the centroid of the quadrilateral $B_1B_2B_3B_4$. Points A_1, A_2, A_3, and A_4, respectively, are the centroids of the four neighboring quadrilaterals of the quadrilateral $B_1B_2B_3B_4$. Q^* marked by a cross in Fig. 2.3(a), is the centroid of the polygon $A_1B_1A_2B_2\ A_3B_3A_4B_4$. Point Q^*, which generally does not coincide with point Q, is referred to as the solution point associated with Q. Note that points A_1^*, A_2^*, A_3^*, and A_4^*, which are also marked by crosses, are the solution points associated with the centroids A_1, A_2, A_3, and A_4, respectively. To proceed, we consider the space-time mesh shown Fig. 2.3(b). Here $t = n\Delta t$ at the nth time level, where n = 0, 1/2, 1, 3/2, … For a given n, Q, Q', and Q'', respectively, denote the points on the n^{th}, the $(n\text{-}1/2)^{\text{th}}$, and $(n+1/2)^{\text{th}}$ time levels with point Q being their common spatial location. Other space-time mesh points in Fig. 2.3(b) are defined similarly. Without going into details of the algorithm, Fig. 2.3(c) represents a three-dimensional spatial mesh of the CESE method for flow in a three-dimensional space. Interested readers could find details of the 3D CESE scheme in [14].

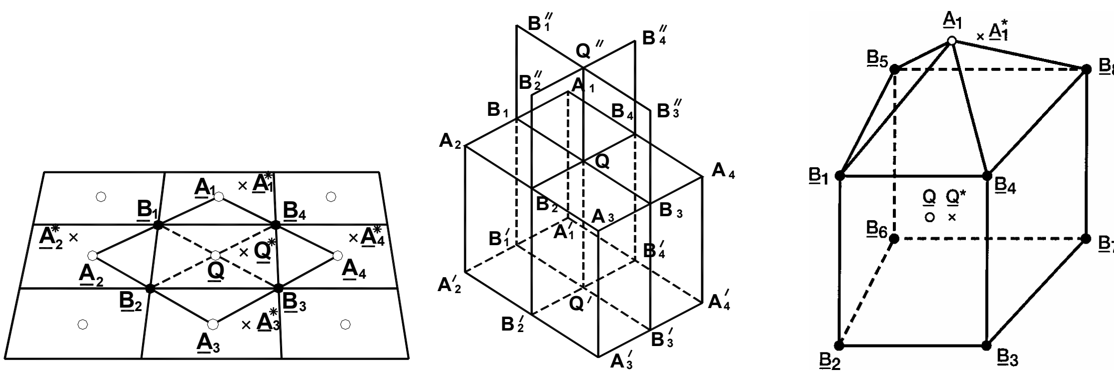

(a) (b) (c)

Fig. 2.3: The space-time mesh in multi spatial dimensions: (a) 2D grid points in the x-y plane, (b) SE and CE for the 2D scheme, (c) 3D grid points in the x-y-z space.

Numerical treatments to achieve non-reflecting boundary condition in conventional CFD methods have been developed based on theorems of the partial differential equation, and they could be categorized into the following three groups: (i) applying the method of characteristics to the discretized equations, (ii) the use of the buffer zone or a perfectly matched layer, and (iii) applying asymptotic analytical solution at the far field. In the setting of the CESE method, we only concern the integral equation and the above ideas of treating non-reflective boundary are not applicable. The non-reflecting boundary condition treatment is based on flux conservation near the computational boundary and letting the flux from the interior domain to smoothly exit to the computational domain through flux balance over boundary CEs. Because each CE allows flux and thus the flow information to be propagated into the future, implementation of this flux-based boundary condition is extremely simple.

III. Results and Discussions

In the numerical simulation, the plasma discharge power input to the flow is simulated as a time-dependent gas temperature disturbance at the inlet boundary of the calculation domain. We assume that the arc discharge between two pin electrodes of a plasma actuator causes a gas temperature pulse. Since the discharge power of the plasma actuator is a step function of time, we introduce a step function disturbance to the gas temperature in the flow. In the current calculation, the discharge power is estimated by the experimentally measured voltage (V) and current (I) data (power = V*I). The gas temperature (T) is calculated by the following equation,

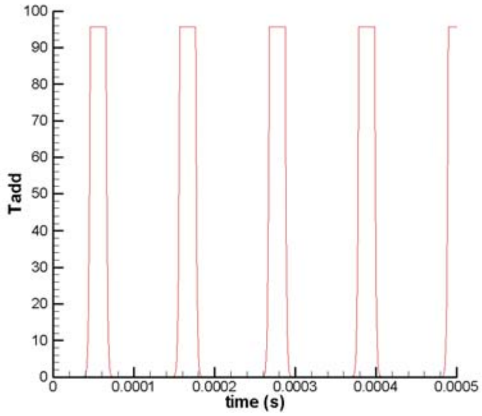

Fig. 3.1: The boundary condition of temperature of one plasma actuator at the nozzle exit perimeter. The frequency of the pulses is 9 kHz.

$$T = {Power}\big/{\rho u A_{arc}} \qquad (3.1)$$

where ρ is gas density, u is gas velocity and A_{arc} is transverse area of arc discharge. The gas temperature disturbance at the inlet boundary is shown in Fig. 3.1. Figure 3.2 shows the three-dimensional mesh, which is composed of about 4.8 millions of hexes. The mesh is clustered near the nozzle exit and free shear layer region. The minimum mesh sizes at the nozzle exit are Δr = 0.0032 *D* (*D* = 25.4 mm is exit diameter of the nozzle) and Δx = 0.0187 *D*, where Δr is the length of the hexes in the radial direction and Δ x is in the axial direction. The maximum cell sizes are Δr = 0.0576 D and Δx =0.0469 *D* at the downstream end of the computational domain.

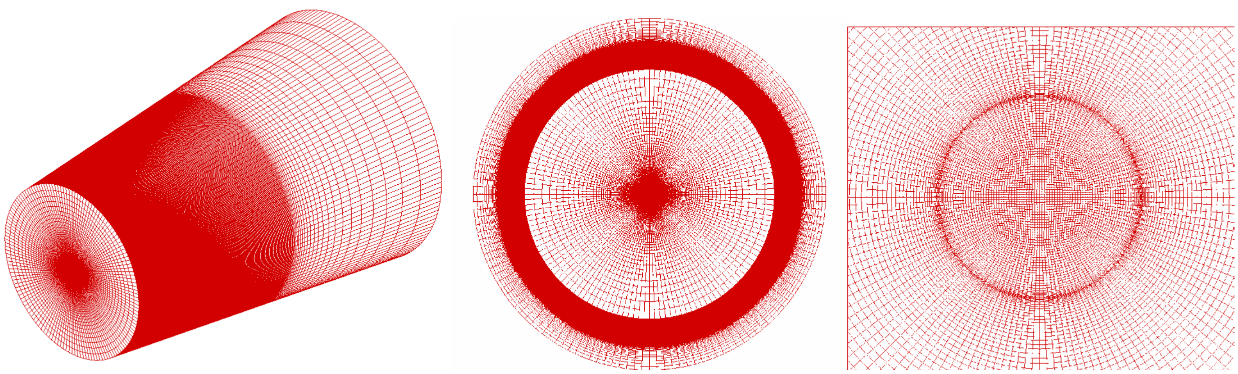

(a) (b) (c)

Fig. 3.2: The three-dimensional mesh of the computational domain.

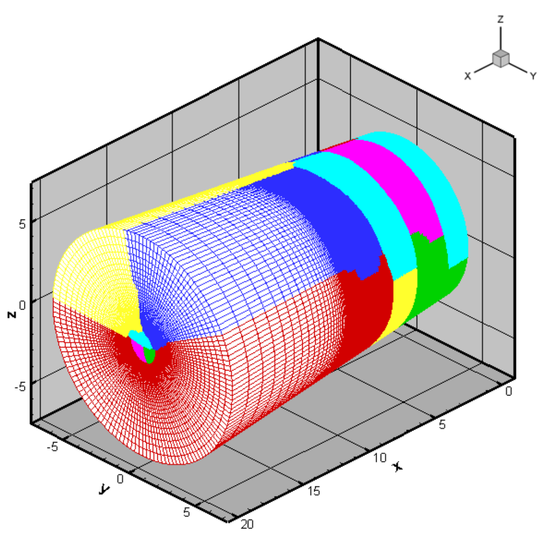

Fig. 3.3: Domain decomposition for parallel computation. Different colors denote the sub-domains calculated by using different CPU nodes.

The unsteady three-dimensional calculations demand significant computer resources. Efficient use of a parallel computer requires proper distribution of simulation tasks over available CPU nodes. We decomposed the computational domain into a number of partitions and assigned the computational tasks in each sub-domain to a computer node. The processing nodes executed the same CESE 3D solver in the sub-domains. At the end of each time step, each processing node communicated with its neighboring nodes and exchanged the intermediate solutions at the sub-domain boundaries. The domain decomposition tool was developed based on (i) balancing the computational workload and memory occupancy among the nodes, and (ii) minimizing the inter-node communication. A set of metrics for characterizing communication cost and load balance were identified by considering the combined effect of the CESE algorithm for solving the Euler equations and the architecture of the cluster computers. The metrics were then used to guide the development of the partitioning algorithm and the CESE code. Figure 3.3 shows the result of automatic domain decomposition of a simple unstructured mesh for the jet flow calculations. The

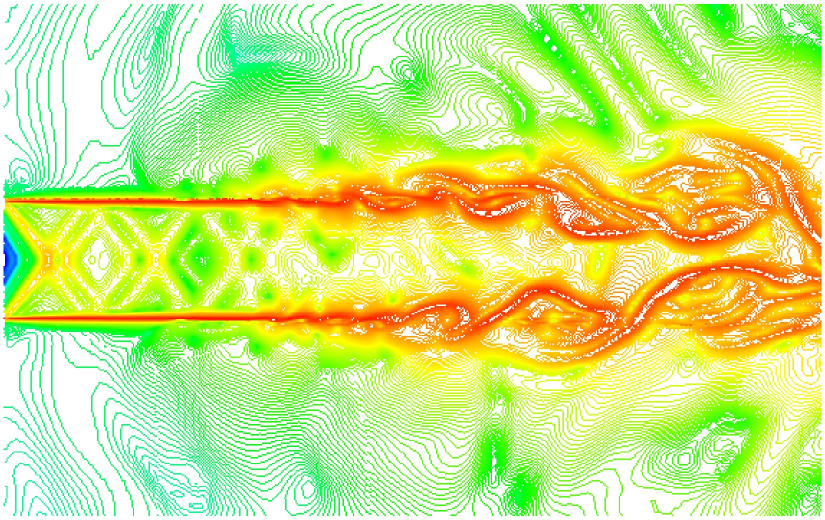

Fig. 3.4: A snapshot of Case (i) jet, the baseline supersonic jet without applying actuators.

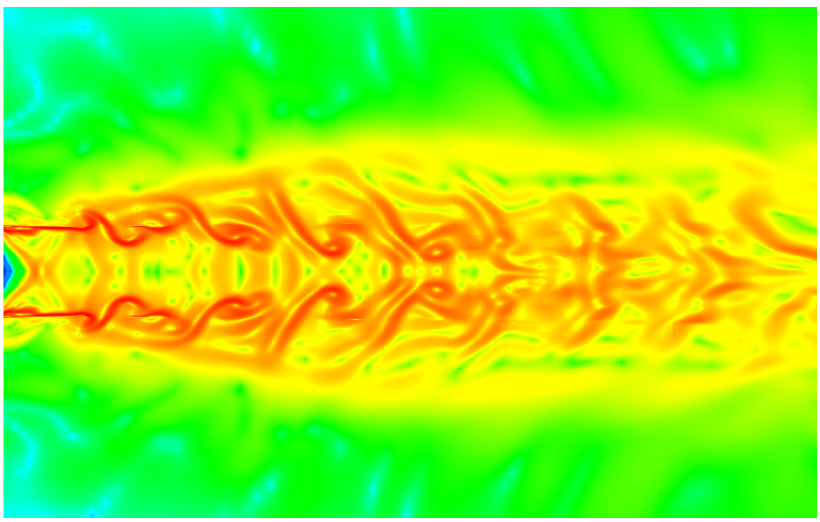

Fig. 3.5: Snapshot of Case (ii) jet at a quasi-stationary stage. Four actuators at 9 kHz with the actuator width at 3 mm are applied.

software package is able to partition the tasks to hundreds of CPU nodes. The present CESE solver is a state-of-the-art modeling code for nonlinear hyperbolic conservation laws.

Figure 3.4 is a snapshot of the baseline supersonic jet. The ambient conditions are the total pressure P_o= 1 atm, the total temperature T_o = 300 K, the total density ρ_o = 1.176 kg/m^3, the specific heat ratio γ= C_p/C_v = 1.41, and the gas constant for air R =287 J/kg-K. The jet conditions are nozzle diameter = 25.4 mm, Mach number = 1.35, pressure P = 1.0066 P_o and ρ =1.355 ρ_o. The result clearly showed that the CESE solver was able to capture salient features of a typical supersonic jet.

Figure 3.5 shows a snapshot of plasma modulated jet. After we obtained the stationary solution of unsteady calculations, we turned on the numerical boundary conditions for the plasma actuators. Figure 3.5 shows the quasi-stationary stage of plasma modulated jet. Figure 3.6 shows an experimental flow visualization image and a snapshot of calculated vorticity contours of the plasma controlled jet. The experimental result shows a phase averaged image of the mixing layer with 8 actuators, operating in first helical mode at 9 kHz. The image clearly shows the distinct flow structures in the controlled jet. The calculated vorticity image shows structures qualitatively similar to the experimental result. Figure 3.7 shows the frontal view of vorticity contours at different axial locations. The counter-rotating vortex pairs were created by the imposed plasma pulses. These organized vortex pairs, in addition to jet column instability structures shown in Fig. 3.6 in [3], perturb the invisicd core of the jet. As a result, the inviscid core length is reduced and the mixing is enhanced. We remark that the experimental results do not show such streamwise vortex pairs because the heating between the electrodes is not uniform.

Figures 3.8(a) and (b) show snapshots of Case (iii) and Case (iv) flows, respectively. The flow conditions of Case (iii) are identical to that in Case (ii) except that the width of each actuator in the azimuthal direction is reduced from 3 mm in Case (ii) to 1.5 mm. Nevertheless, the flow structure is about the same as that in Case (ii). In Case (iv), the actuator width remains to be 3 mm but the frequency of the applied plasma pulses has been reduced to be 4.5 kHz. Figure 3.8(b) shows that Case (iv) jet has a more random and less synchronized flow structure as compared to that of Cases (ii) and (iii).

Figure 3.9 shows the averaged axial Mach number profiles at various axial locations. The most striking feature is that at L/D = 4, 6, and 8, the Mach number profiles of Case (ii) and (iii) show a distinct plateau in the middle of the supposed parabolic profile commonly seen in unperturbed jets. The apparent flatness of the axial Mach number

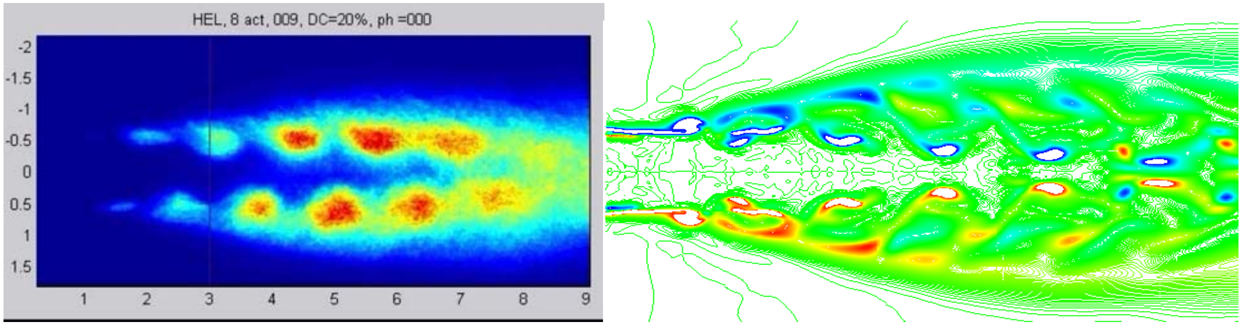

(a) (b)

Fig. 3.6: Comparison between (a) the experimental result and (b) the calculated vorticity contours.

profiles in the middle of the profile is mainly caused by the vortex pairs as shown in Fig. 3.7. At *L/D* = 2, the vortex pairs are very narrow around the nozzle periphery. Refer to Fig. 3.7 (a). Thus the Mach number profiles were less affected. At *L/D* =10, the jet is fully mixed, and one cannot discern the flat plateau.

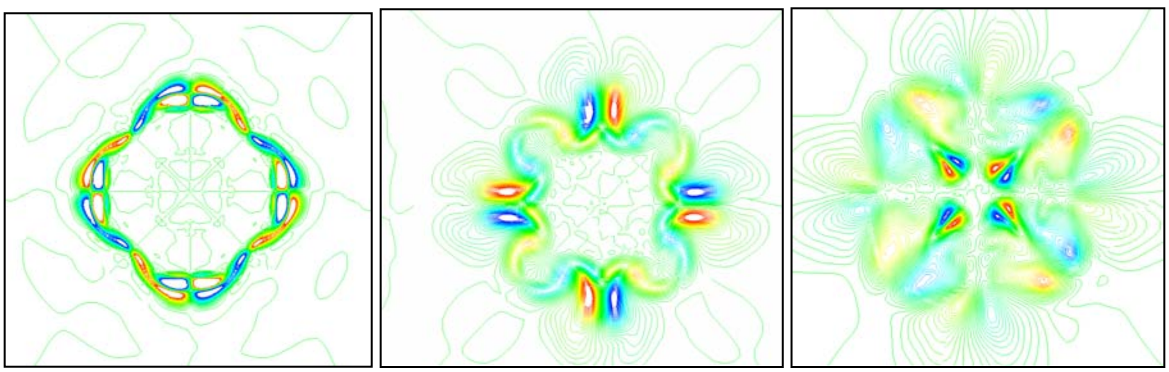

Fig. 3.7: Calculated vorticity contours of Case (ii) jet on the planes at three axial locations: *L/D* = 1, 3, and 5.

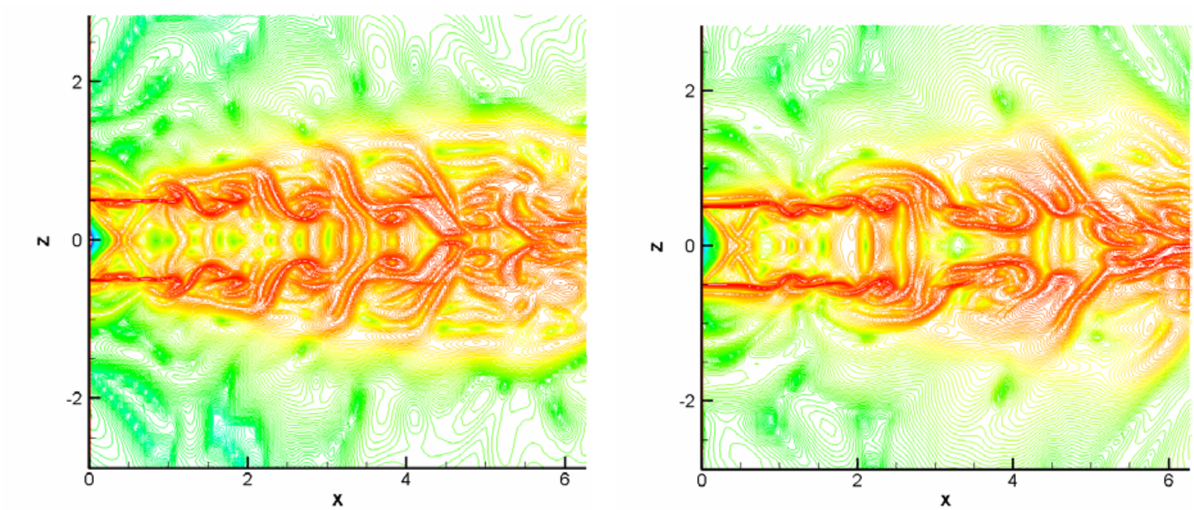

(a) (b)

Fig. 3.8: Snapshots of (a) Case (iii) jet and (b) Case (iv) jet.

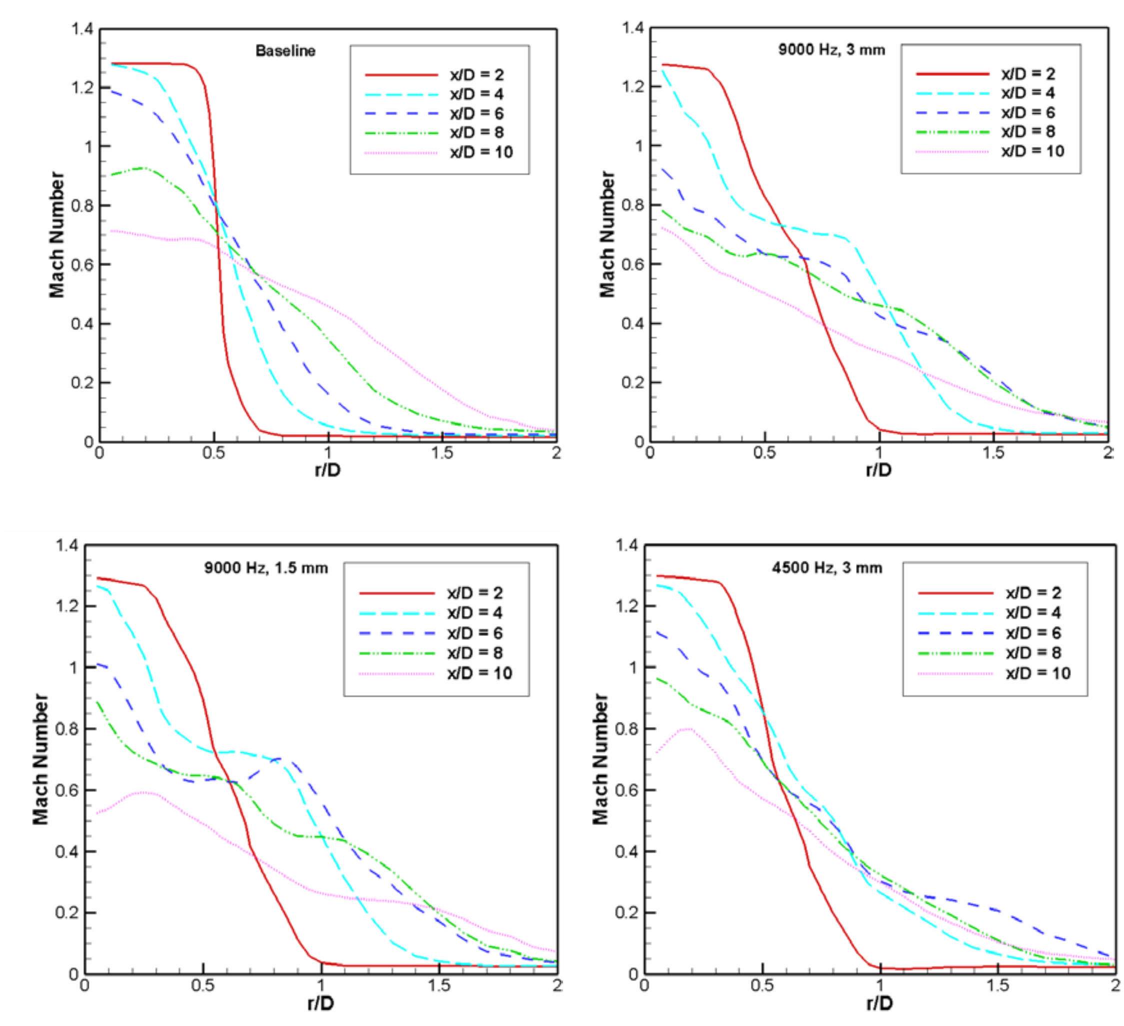

Fig. 3.9: Averaged axial Mach number profiles at different axial locations for the four cases.

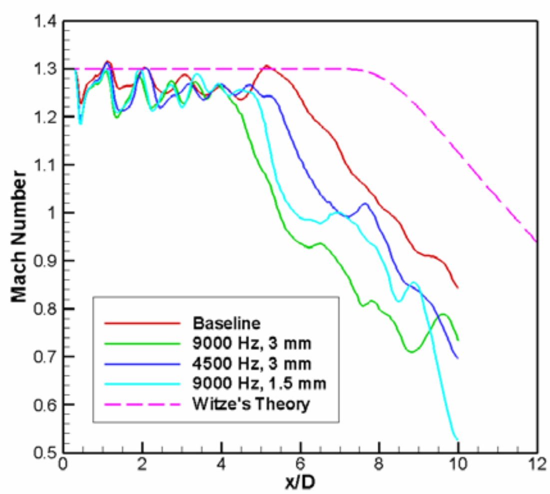

Fig. 3.10: Streamwise Mach number profile of four cases compared with Witze's correlation [16].

Figure 3.10 shows the averaged axial Mach number profiles of the four calculated jets compared with an empirical correlation for the centerline velocity decay proposed by Witze [16]. In general, the calculated inviscid core length of Case (i) the baseline jet is shorter than that calculated by using Witze's formulation [16]. This is probably due to lack of mesh resolution at the downstream of the computational domain. Further refining the mesh and better control of the numerical damping in the calculation will be needed to improve the simulation results. Nevertheless, CFD results clearly capture the qualitative trend of the centerline velocity decay of the fours cases. In general, Cases (ii-iv), with plasma actuators turned on, have shorter inviscid cores as compared to Case (i) the baseline jet. Among the controlled jets, Case (ii) has the shortest inviscid core. Comparison between Case (iii) and (iv) shows that the frequency effect is more important than the size of the actuators for the same amount of the applied plasma energy.

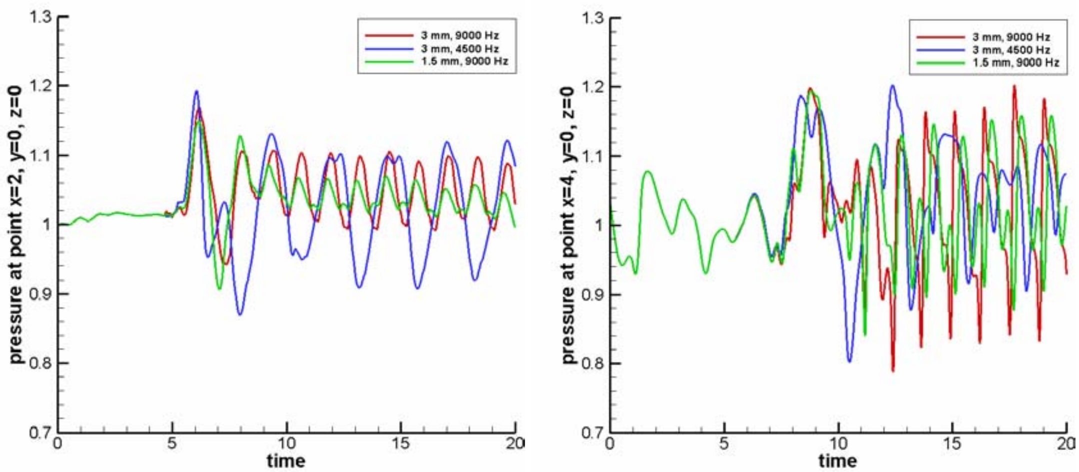

(a) *L/D* = 2 (b) *L/D* = 4

Fig. 3.11: Histories of pressure fluctuations at two centerline locations: *L/D*= 2 and 4.

Figure 3.11 shows the histories of pressure fluctuations at two centerline locations: *L/D* = 2 and 4. At *L/D*= 2, pressure fluctuations are dominated by the nearby actuators. In Case (iii), the amplitude of pressure fluctuations, denoted by a green line, is less than that of Case (ii), denoted by a red line, owing to smaller actuators employed. On the other hand, the amplitude of pressure fluctuations of Case (iv) of 4.5 kHz, denoted by a blue line, is significantly larger due to longer intermittence for gas to respond to the imposed perturbations. At *L/D* = 4, the amplitudes of pressure fluctuation of both Cases (ii) and (iii) grow significantly with their wave pattern and frequency resemble that at L/D =2. However, the wave pattern of Case (iv) of 4.5 kHz at *L/D* = 4 becomes quite chaotic and little growth in the amplitude can be observed.

IV. Conclusion

In this paper, we have reported direct calculations of an ideally expanded supersonic axisymmetric jet controlled by localized arc filament plasma actuators. The CESE method was employed to solve the three-dimensional Euler equations with and without the application of plasma actuators. The CESE code is a totally unstructured mesh solver and fully parallelized for efficient computations. We simulated four actuators distributed around the perimeter of a 2.54 mm diameter axisymmetric nozzle by imposing energy pulses at 9 kHz and 4.5 kHz. Numerical results of four cases are reported: (i) the baseline case without control, (ii) simultaneous firings of four actuators at 9 kHz with the width (in the azimuthal direction) of each actuator at 3 mm, (iii) same as (ii) expect the actuator width at 1.5 mm, and (iv) same as (ii) except firing at 4.5 kHz. The results have been studied by snapshots of flow field in planar and frontal views, averaged Mach number profiles on the cross-section planes at various axial locations, and averaged centerline velocity decay rate. For Cases (ii) to (iii), numerical results clearly showed robust and spatially coherent structures generated in the controlled jet leading to tremendous mixing enhancement. Case (iv), on the other hand, shows less effective mixing and more chaotic flow structure as compared to Cases (ii) and (iii).

References

1. Samimy, M., Kim, J.-H., Adamovich, I., Utkin, Y. and Kastner, J., “Active Control of High Speed and High Reynolds Number Free Jets Using Plasma Actuators”, AIAA Paper 2006-0711.
2. Samimy, M., Kim, J.-H., Adamovich, I., Utkin, Y., and Keshav, S., “High Speed Jet Control Using Plasma Actuators,” 4th International Symposium on Turbulence and Shear Flow Phenomena, Williamsburg, Virginia, June 2005.
3. Samimy, M., Adamovich, I., Webb, B., Kastner, J., Hileman, J., Keshav, S., and Palm, P., “Development and Characterization of Plasma Actuators for High Speed and Reynolds Number Jet Control,” Experiments in Fluids, Vol. 37, No. 4, pp. 577-588, 2004b.
4. Chang, S. C., 1995, "The Method of Space-Time Conservation Element and Solution Element-a New Approach for Solving the Navier-Stokes and the Euler Equations," Journal of Computational Physics, Vol. 119, pp. 295.
5. Chang, S. C., Wang, X. Y., and Chow, C. Y., 1999, "The Space-Time Conservation Element and Solution Element Method: A New High-Resolution and Genuinely Multidimensional Paradigm for Solving Conservation Laws," Journal of Computational Physics, Vol. 156, pp. 89.
6. Chang, S. C., Wang, X. Y., and To, W. M., 2000, "Application of the Space-Time Conservation Element and Solution Element Method to One-Dimensional Convection-Diffusion Problems," Journal of Computational Physics, Vol. 165, pp. 189.
7. Chang, S. C., Yu, S. T., Himansu, A., Wang, X. Y., and Loh, C. Y., 1999, "The Method of Space-Time Conservation Element and Solution Element --a New Paradigm for Numerical Solution of Conservation Laws," Computational Fluid Dynamics Review 1998, pp. 206-240.
8. Im, K.-S., Lai, M.-C., Yu, S.-T. J., and Jr., R. R. M., 2004, "Simulation of Spray Transfer Processes in Electrostatic Rotary Bell Sprayer," Journal of Fluids Engineering, Vol. 126(3), pp. 449-456.
9. Im, K.-S., Yu, S.-T. J., M. -C. Lai, and Meredith, W. H., 2003, "Simulation of the Shaping Air Flows and Spray Transport in Electrostatic Rotary Bell Painting Processes," Journal of Material Manufacturing, SAE Transactions, Vol. 110(5), pp. 965-975.
10. Kim, C.-K., Yu, S.-T. J., and Zhang, Z., 2004, "Direct Calculation of High-Speed Cavity Flows in a Scramjet Engine by the CESE Method," AIAA Journal, Vol. 42(5), pp. 912-919.
11. Qin, J. R., Yu, S.-T. J., and Lai, M. C., 2001, "Direct Calculations of Cavitating Flows in Fuel Delivery Pipe by the Space-Time Cese Method," Journal of Fuels and Lubricants, SAE Transaction, Vol. 10814, pp. 1720-1725.
12. Wang, X. Y. and Chang, S. C., 1999, "A Two-dimensional Non-Splitting Unstructured Triangular Mesh Euler Solver Based on the Space-Time Conservation Element and Solution Element Method," International Journal of Computational Fluid Dynamics, Vol. 8(2), pp. 309.
13. Yang, D., Yu, S.-T. J., and Zhao, J., 2001, "Convergence and Error Bound Analysis for the Space-Time Cese Method," Numerical Methods for Partial Differential Equations, Vol. 17, pp. 64-78.
14. Zhang, Z., Yu, S.-T., and Chang, S. C., 2002, "A Space-Time CESE Method for Solving the Two- and Three-Dimensional Unsteady Euler Equations Using Quad and Hex Meshes," Journal of Computational Physics, Vol. 175, pp. 168-199
15. Wang, B., He, H., and Yu, S.-T. John, 2005, “Direct Calculation of Wave Implosion for Detonation Initiation,” AIAA J., Vol. 43, No. 1, pp. 2157-2169.
16. Witze, P. O., 1974, “Centerline Velocity Decay of Compressible Free Jets,” AIAA J., Vol. 12, No. 4, pp. 417-418.